Reproducible Acquisition of *Escherichia coli* Porin Surface Topographs by Atomic Force Microscopy

Frank A. Schabert and Andreas Engel
Maurice E.-Müller Institute for Microscopic Structure Biology Biozentrum, University of Basel, CH-4056 Basel, Switzerland

ABSTRACT Crystalline membranes reconstituted from *Escherichia coli* OmpF porin and phospholipids were adsorbed to freshly cleaved mica and imaged in solution by the atomic force microscope. The extracellular as well as the periplasmic side of the porin trimers could be identified and the conditions to record topographs at 1-nm lateral and 0.1-nm vertical resolution were established.

INTRODUCTION

The atomic force microscope (AFM) (Binnig and Quate, 1986) is the most prominent instrument among the scanning probe microscopes, which is capable of imaging insulating surfaces at high resolution. It circumvents metal coating necessary for reliable imaging of biological samples by the scanning tunneling microscope (STM) (Binnig and Rohrer, 1982; Amrein, 1989; Stemmer et al., 1989; Engel, 1991; Guckenberger et al., 1991). Atomic resolution imaging of solid-liquid interfaces (Manne et al., 1991) and molecular resolution imaging of protein surfaces by the AFM has been demonstrated (Hoh et al., 1993; Karrasch et al., 1993, 1994; Yang et al., 1993, 1994a, b). In addition, biological processes have been monitored by the AFM (Drake et al., 1989). To explore its capabilities for the analysis of integral membrane proteins, we have studied the *Escherichia coli* membrane protein OmpF.

OmpF porin is a major protein of the outer membrane of *E. coli* that is present as a trimer and functions as a molecular sieve allowing passage of molecules up to 600 Da. OmpF porin is one of the few membrane proteins solved to 2.4 Å resolution by x-ray crystallography (Cowan et al., 1992). Each of the three pores of a trimer consists of a cylindrical sheet of antiparallel β strands that are connected by short loops on the smooth side of the cylinder and loops of variable length on the rough side, which has been identified as extracellular (Hoenger et al., 1993b). The disposition of aromatic residues (primarily tyrosine, with hydroxy groups pointing toward the hydrophilic moiety (Cowan et al., 1992)) suggests that the smooth side of the trimers is flush with the periplasmic bilayer surface and that the long loops on the extracellular surface result in corrugations of >1 nm depth. In the presence of phospholipids, purified OmpF-lipopolysaccharides (LPS) complexes readily crystallize into a rectangular, double-layered, 2D crystal with unit cell dimensions $a = 8.2$ nm, $b = 13.8$ nm, and two types of trigonal 2D crystals, exhibiting unit cell dimensions of $a = b = 9.3$ nm, and $a = b = 8.2$ nm, respectively (Dorset et al., 1983; Hoenger et al., 1990).

Here we describe the conditions established by systematic experimental analysis that allow topographs of OmpF porin lattices to be acquired in solution at subnanometer resolution.

MATERIALS AND METHODS

Specimen preparation

OmpF porin trimers were isolated from an *E. coli* B^e strain as described (Hoenger et al., 1993a). For assembly into 2D lattices, porin trimers solubilized in octylpolyoxyethylene were mixed with solubilized dimyristoyl phosphatidylcholine (99% purity, Sigma Chemical Co., St. Louis, MO) at a lipid-to-protein ratio (w/w) of 0.2 and a protein concentration of 1 mg/ml. OmpF-LPS complexes with either two loosely and one tightly bound LPS molecule per porin trimer or with no loosely bound LPS were reconstituted by eliminating the detergent in a temperature-controlled dialysis device (Jap et al., 1992).

Mica discs of 5 mm diameter were glued with a two-component glue onto 10 mm diameter Teflon supports that were mounted on magnetic sample holders for the AFM (see Fig. 1). Freshly cleaved mica was preincubated with 20 μl dialysis buffer (100 mM NaCl, 20 mM HEPES, 2 mM $MgCl_2$, pH 7.0) for 5 min. After removing the buffer, 1–3 μl of sample solution were added, and after 10 min the sample was washed three times with dialysis buffer to remove membranes that were not firmly adsorbed to the substrate.

Atomic force microscopy: instrumentation and operation

A commercial AFM (Nanoscope III, Digital Instruments, Santa Barbara, CA) equipped with a 150-μm scanner (j-scanner, Digital Instruments) and a liquid cell was used. By reducing the maximum voltage driving the z-electrode of the piezo from 440 to 55–100 V the instrumental axial resolution was increased and operation was more stable. Either the height signal of trace and retrace scan, or height and cantilever deflection signal, were acquired in parallel in 512 × 512 pixel frames. Oxide-sharpened Si_3N_4 cantilevers with 120-μm length and a nominal spring constant of $k = 0.38$ N/m or oxide-sharpened Olympus tips ($k = 0.1$ N/m, purchased from Digital Instruments) were used. To reduce the mechanical load on the piezo scanner, and to avoid contact of the buffer with different surfaces as much as possible, scanning was performed without the use of the O-ring for sealing. 20–50 μl of buffer was found to be sufficient for stable operation of the AFM over several hours. All buffer solutions used were filtered through 0.2-μm pore size-filter membranes (Millipore, Bedford, MA).

The fast scan direction was set at an angle of 90° with respect to the axis of the cantilever. The forces were kept as small as possible, significantly below 1 nN. ~1 h after changing samples or cantilevers, the thermal drift

---

Received for publication 7 July 1994 and in final form 14 September 1994.

Address reprint requests to Dr. Andreas Engel, M.E. Müller Institute, Biozentrum, University of Basel, Klingelbergstrasse 70, CH-4056 Basel, Switzerland. Fax: 0041-61-267-22-59; E-mail: aengel@urz.unibas.ch.

0006-3495/94/12/2394/10 $2.00

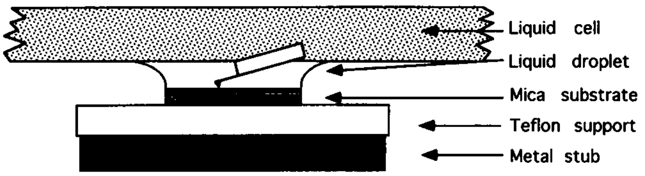

FIGURE 1 Sample holder. A mica disc is fixed on a Teflon support using a two-component glue. The Teflon support is glued onto a magnetic metal stub that is mounted on the piezo tube scanner. The liquid cell consists of a transparent glass slab to which the cantilever is mounted. The liquid droplet minimizes the contact to the hydrophobic Teflon by forming a meniscus to the glass surface of the liquid cell.

of the zero force deflection angle of the cantilever was typically 0.3 nm/min. Therefore, the deflection setpoint needed to be adjusted during image acquisition. This often resulted in a few distorted scan lines, but allowed operation at forces <200 pN. Gains were set by increasing the integral gain before setting the proportional gain. Both were carefully optimized to prevent oscillations even at minimum forces. The scan speed was optimized for each topograph individually to simultaneously minimize the deflection signal and the influence of drift phenomena and creep of the scanner. Typically, the scan speed was set to 4 lines/s (2-Hz line frequency, twice trace and retrace per s) for all scan sizes and sometimes reduced to 2 or 3 lines/s for large-scale scans.

Image analysis

For image processing, all raw data were transferred to a VAX 3100 workstation and analyzed using the SEMPER software (Saxton et al., 1979) (Synoptics Ltd., Cambridge, UK). Images were flattened line by line, Fourier transformed, cross-correlated, and averaged as described (Saxton and Baumeister, 1982). Trace and retrace topographs that were acquired in parallel were cross-correlated to determine their translational offset and added to eliminate contributions of friction to the topography (Grafstöm et al., 1993, 1994; Radmacher et al., 1992; Schabert et al., 1994). For correlation averaging, a well-preserved unit cell was selected from the raw data and cross-correlated with the topograph (Saxton and Baumeister, 1982). Correlation peaks identified the position of the unit cells within the 2D crystal and allowed lattice distortions to be unbent by fitting spline functions through the peaks and resampling the image along curvilinear coordinates (Saxton et al., 1992). Unit cells were then extracted according to the peak coordinates and averaged. The resulting correlation average was used as reference for refinement cycles (Saxton et al., 1984). Single-unit cells were also processed as single particles, i. e., they were aligned angularly as well as translationally before averaging (Frank et al., 1978). To assess the precision of the height data not only the average $\mu_{k,l}$ but also the root mean square deviation RMS = σ_{kl}, where

$$\sigma_{k,l}^2 = \frac{1}{N}\sum_{i-1}^{N}(x_{kl}^i - \mu_{k,l})^2$$

was calculated for each pixel (k, l) for particles x^i (Karrasch et al., 1994). To assess the lateral resolution, three criteria were used. First the Fourier ring correlation function (RCF; Saxton and Baumeister, 1982) was calculated from the transforms F_1 and F_2 of two independent averages

$$\mathrm{RCF}(k) = \frac{\sum_k [F_1(k)F_2 * (k)]}{\sqrt{\sum_k |F_1(k)|^2 \sum_k |F_2(k)|^2}}$$

In this case, the resolution limit is defined as crossover of the RCF with the function $2/\sqrt{n_k}$, where n_k is the number of Fourier orders in a ring segment of radius k. Second, the phase residual (PR; (Frank et al., 1981) was calculated according to

$$\mathrm{PR}(k) = \overline{\Delta\theta(k)} = \sqrt{\frac{\sum\{[|F_1(k)| + |F_2(k)|]\Delta\theta_{12}^2(k)\}}{\sum_k\{|F_1(k)| + |F_2(k)|]}}$$

where sums are taken over ring-shaped areas at a distance of k from the origin in Fourier space. $\theta_{12}(k)$ denotes the phase difference between corresponding Fourier components $F_1(k)$ and $F_2(k)$. In this case, the resolution limit is given by an upper value of the PR of 45°. Third, the estimated spectral signal power

$$\mathrm{SS}(k) = \sum_k |F_1 + F_2|^2$$

is compared with the spectral noise power following Unser et al. (1987):

$$\mathrm{SN}(k) = \sum_k |F_1 - F_2|^2.$$

In this case, the resolution limit is given by the crossover between SS and 4 * SN.

RESULTS

Morphology and resolution criteria

Reconstituted 2D OmpF lattices form sheet-like structures of up to 10 μm in diameter, which adsorbed to mica in the presence of Mg^{2+} ions (see Fig. 2). The sample was first scanned at low magnification (typically 50–100-μm scan size) to locate areas of interest. Patches of OmpF porin membranes were identified by their morphology in the error signal mode (Putman et al., 1992). Edges of the porin sheets were clearly seen in the deflection signal, whereas the height signal allowed single, double, or multiple layers to be identified. Sheets of pure phospholipids were frequently found but were easily recognized because they were less stable due to their

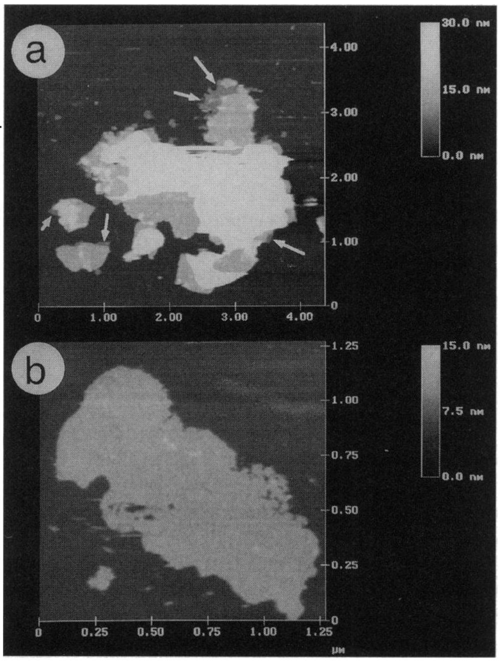

FIGURE 2 OmpF porin sheets imaged with the AFM at low magnification. (*a*) Reconstituted *E. coli* porin OmpF sheets usually form double layers. Regions that adsorbed to the mica substrate are sufficiently stable to be scanned with the AFM. Central regions where multiple layers are stacked exhibit some instabilities. Arrows mark positions where the double layers do not overlap perfectly and terraces with the extracellular side of single layers are exposed. (*b*) Monolayer of reconstituted porin sheet, with the extracellular side of the porin trimer exposed to the tip.

high lateral fluidity. In addition, zooming in to high magnification resulted in the destruction and displacement of phospholipid bilayers.

Fig. 2 *a* shows a double layer of porin sheets adsorbed to the mica substrate with flat regions that were stable and other regions that were not firmly attached and therefore not sufficiently stable for imaging. As an alternative to the mica substrate, glass coverslips that were functionalized with photoreactive crosslinkers were used as carriers (Karrasch et al., 1993), but the membranes appeared to be more wrinkled than when adsorbed to mica (data not shown). OmpF porin sheets reconstituted at a lipid-to-protein ratio (LPR) of 0.2 usually form double layers (Engel et al., 1985) with the extracellular sides sandwiched between the periplasmic sides (Hoenger et al., 1993b). Therefore, the extracellular sides were in general not accessible to the tip. We used different approaches to circumvent this:

First, the two layers often did not perfectly overlap. Thus, terraces of monolayers were found, where small regions of the extracellular side of the bottom layer were exposed (Fig. 2 *a*, arrows). Second, monolayers could be found that comprised protein patches in lipid bilayers with a low degree of crystal order (Fig. 2 *b*). Third, by scanning the upper layer at its edge with slightly increased force, it could be dislodged, thereby exposing the lower layer.

At higher magnification, individual porin trimers were easily recognized on topographs without further processing of the data (Fig. 3). The two sides of the OmpF porin trimer could be distinguished based on their morphology. The trimers of the friction-corrected raw data (a selection is shown in Fig. 4 *c*–*r*) were aligned angularly and translationally before averaging (Frank et al., 1978) to eliminate misalignments due to lattice line bending. All the trimers analyzed were also split into independent sets and averaged in parallel (Fig. 4, *s iii* and *iv*, and *t iii* and *iv*) to be compared by Fourier RCF analysis (Saxton and Baumeister, 1982) (see also Fig. 7, *a* and *b*). The overall average (Fig. 4, *s* and *t*) and RMS deviation maps (Karrasch et al., 1994) (Fig. 4, *s ii*, and *t ii*) were calculated, to provide height values as well as a quantitative assessment of their reproducibility. In Fig. 4 *b*, the position of the trimers that were used for averaging are marked. Two lattices can be seen that exhibit different angular orientations. The averages calculated from these two domains of the crystal (Fig. 4, *s* and *t*) show the trimers in different orientations but with similar morphology. The average trimers exhibit sharp features in the center with a protrusion about the threefold axis, whereas the structure smears out rapidly with increasing distance from the center as a result of the lattice distortions. This is also visible on the RMS deviation maps, which have larger values at their periphery. In addition to changes of the orientation, which can be compensated by angular alignment of the particles, bending of the lattice also distorts the particles. The lattice distortion displayed in Fig. 5 *a* was corrected in Fig. 5 *b* (Saxton et al., 1992), yielding a power spectrum with sharper diffraction spots (Fig. 5 *b*, inset) than those derived from the distorted image (Fig. 5 *a*, inset). After lattice unbending, diffraction spots up to the fifth order in the direction of the ⅛-nm lattice vector were visible, suggesting a resolution of 1.6 nm, although the appearance of the image did not change

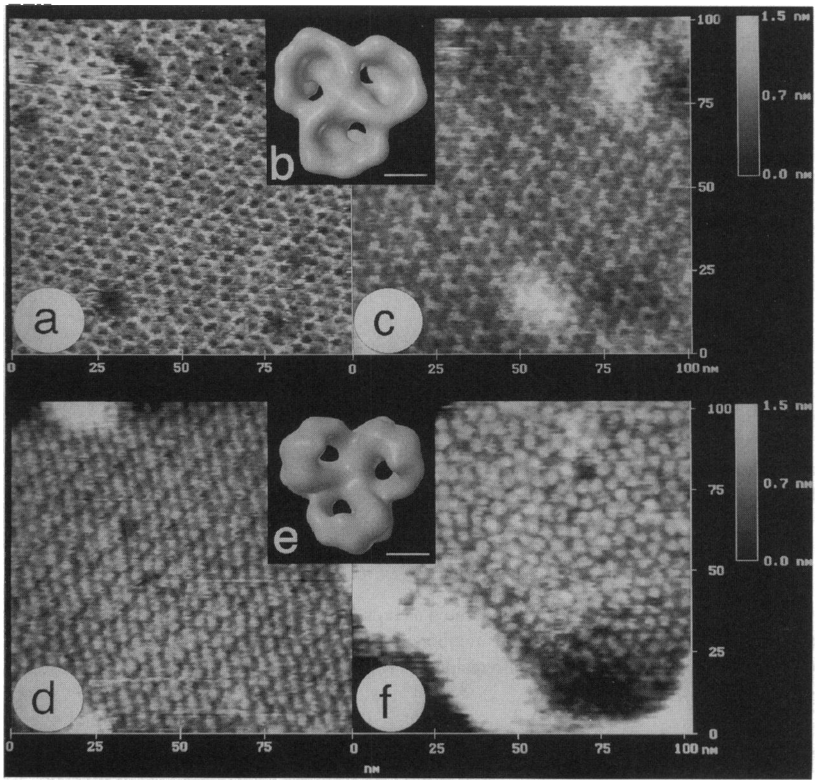

FIGURE 3 Morphology of the periplasmic and extracellular side of OmpF porin trimers in the AFM. The topographs on the left side show rectangular crystals reconstituted without the loosely bound LPS molecules. The hexagonal crystals on the right side consist of porin trimers with two loosely bound LPS molecules. The images of the porin trimer in the center were generated from the atomic structure (Cowan et al., 1992). (*a*) Unprocessed AFM topograph taken on the periplasmic side. The porin trimers are arranged in a rectangular lattice with a = 8 nm and b = 14 nm. Three pores per trimer can be seen. (*b*) The periplasmic side of the OmpF porin trimer surface rendered to 1.5-nm resolution. The scale bar represents 2 nm. (*c*) Unprocessed topograph of the periplasmic side of a crystal comprising OmpF trimers with two loosely bound LPS molecules packed in a hexagonal lattice with $a = b = 9$ nm. (*d*) Extracellular side of the porin trimer reconstituted under the same conditions as in (*a*). (*e*) Extracellular side of the porin trimer rendered to 1.5-nm resolution. The scale bar represents 2 nm. (*f*) Extracellular side of the same crystal as displayed in (*c*).

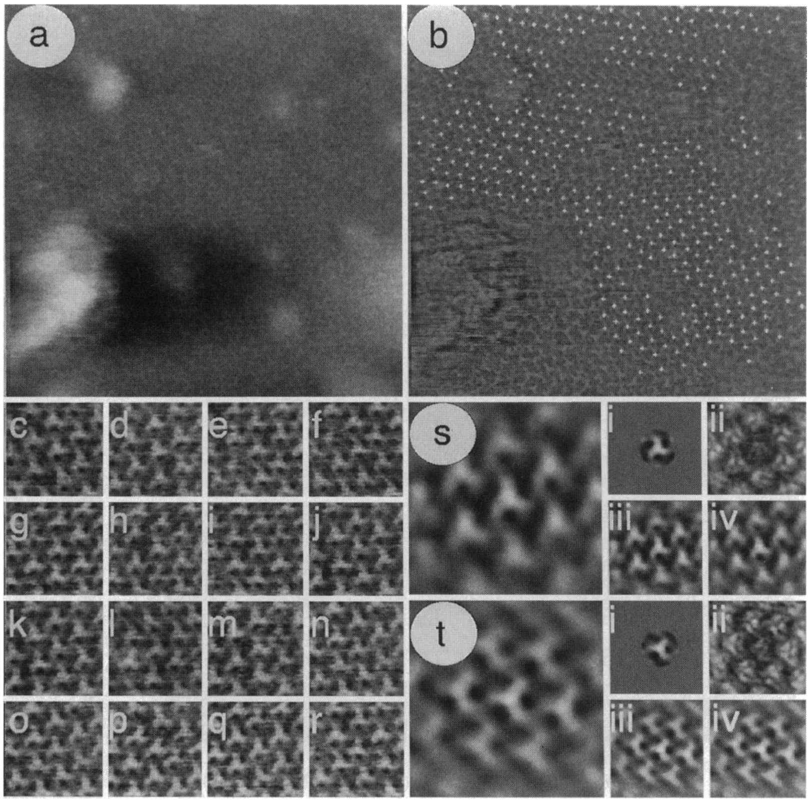

FIGURE 4 Single-particle averaging of an AFM topograph. (*a*) AFM topograph of the periplasmic side of hexagonally arranged trimers reconstituted in the presence of loosely bound LPS molecules. Trace and retrace images were added to eliminate friction effects. (*b*) Positions of the trimers within the topograph are shown, as obtained by cross-correlation with two different references selected from the different regions. Two hexagonal domains can be seen, which are rotated with respect to each other. The positions are overlaid to the high-pass-filtered topograph of (*a*). (*c–r*) Selection of particles that were extracted from the lower right domain of (*a*) according to the positions marked in (*b*). The average calculated from all the particles selected without alignment (*s i*) served as reference for rotational and translational alignment for single-particle averaging. Parts that are not considered for alignment were masked. The overall average (*s*), the RMS deviation map (*s ii*) and two independent averages (*s iii* and *iv*) were calculated. (*t*) shows the overall average as obtained from the other crystal domain, whereas (*t i–t iv*) present the corresponding reference, RMS deviation maps and independent averages. Frames (*a*) and (*b*) are 250 nm wide, whereas all other frames are 31 nm wide.

significantly. Two different trimer orientations present in the rectangular lattice (Fig. 5 *b*) were chosen to calculate two averages shown in Fig. 6 *a* and *b* using single-particle averaging in analogy to Fig. 4. The averages exhibited the same morphology in different orientations with respect to the scanning tip. According to the RMS deviation maps (Fig. 6, *c* and *d*), the RMS deviation was found to be <0.1 nm in the center of the trimer and on the surrounding bilayer, but increased to 0.5 nm in adjacent porin trimers, predominantely in the channels. Similarly, RMS values >0.2 nm were present in the pores and on one of the three walls separating the channels. The latter appeared slightly deformed in the averages, whereas the depth of the pores critically depended on the tip geometry. After rotational and translational alignment, the sum (Fig. 6 *e*) of both averages emphasized those structures that were common to both orientations. The map displaying the modulus of the difference (Fig. 6 *f*) revealed the contributions of tip asymmetry and of nonlinear friction effects to the topographs. Maxima (0.3 nm) occurred again in the pores and furthermore at positions exhibiting a steep gradient (Fig. 6 *d*).

The lateral resolution can be assessed by comparing independent averages, such as displayed in Fig. 4, *s* and *t*. Three criteria have been used (cf. Materials and Methods) that produced similar values for porin trimers in one orientation for the highest spatial frequency $k_{\max}$ carrying significant information on the object studied. First, Fourier ring cross-correlation values were plotted versus the spatial frequency *k* and compared with a theoretical noise estimate (Saxton and Baumeister, 1982) (Fig. 7, *a* and *b*). This resulted in a resolution of 0.8 and 0.9 nm, for the "up" and "down" orientation of porin trimers arranged in a rectangular unit cell, respectively. Second, the comparison of the spectral power (SP) with the spectral noise (SN) (Unser et al., 1987) yielded a resolution of 0.9 and 1.2 nm, respectively (Fig. 7, *c* and *d*). Third, the PR (Frank et al., 1981) was found to cross the 45° limit at 1.2 and 1.3 nm, respectively (Fig. 7, *e* and *f*). The PR calculated from independent averages of the up orientation also exhibited two dips to 50°, one at 0.9-nm resolution (Fig. 7 *e*). Last but not least, trimers in up and down orientations can also be considered as independent averages and be used to assess the resolution after angular alignment. This produced resolution limits of 1.5 nm (RCF; Fig. 7 *g*) and 1.8 nm (SP/SN; Fig., 7 *h*), respectively.

Imaging conditions

In scanning probe microscopy (SPM), the tip geometry is the most critical but the least controlled element. We have tested conventional Si_3N_4 pyramid-shaped tips, Si_3N_4 oxide-sharpened tips, and electron beam-deposited tips. The oxide-sharpened tips gave the best performance, but their properties were found to vary considerably. Double- or multiple-tip effects and tip astigmatism were much more frequent than with other tips. Therefore, tips were selected qualitatively using different assays. Since a hysteresis in the retracting force curves may indicate a contamination of the tip by adsorbed material, tips were selected that did not exhibit the hysteresis when tested on plain mica substrate. Also, the stick-and-slip effect that occurs after the cantilever changes

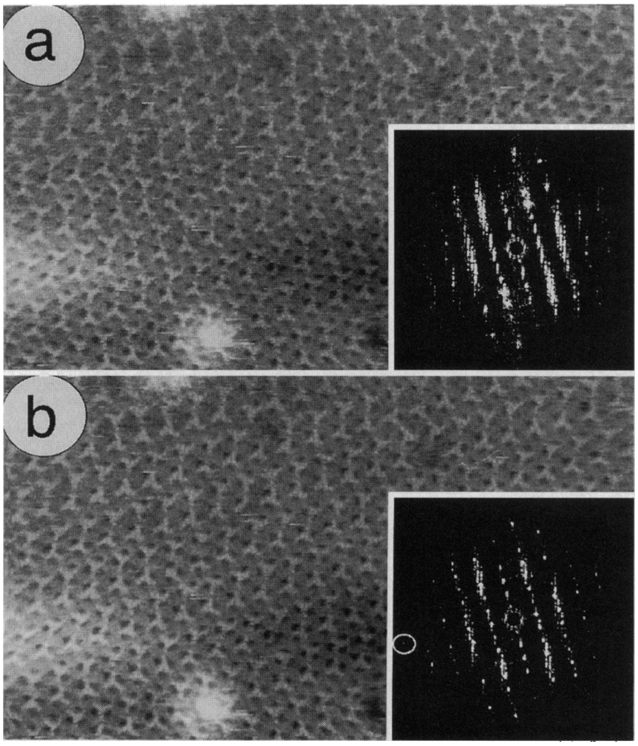

FIGURE 5 Unbending of distorted lattices. (*a*) The AFM topograph reveals that the rectangular lattice was bent. Simultaneously acquired trace and retrace images were added to compensate for friction effects. Spots in the power spectrum (inset), indicating the periodic structure of the topograph, are smeared out. (*b*) Unbending resulted in topograph (*b*), with a power spectrum (inset), which shows sharper peaks that indicate a better crystal order. The ring marks the diffraction order (5.0) at a resolution of $(1.6\ \text{nm})^{-1}$. Frames (*a*) and (*b*) are 200 nm wide.

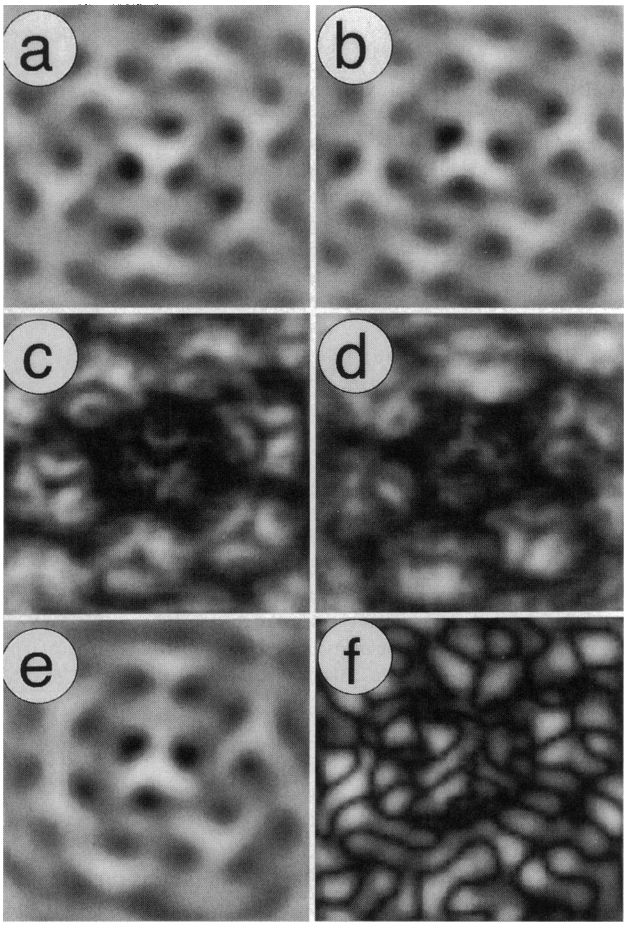

FIGURE 6 Averages of the periplasmic side of a rectangular porin lattice. The porin trimers are arranged in two different orientations. (*a*) and (*b*) Each orientation is analyzed with single-particle averaging. (*c*) RMS deviation map of (*a*). (*d*) RMS deviation map of (*b*). (*e*) Both averages (*a*) and (*b*) were rotationally and translationally aligned and added. (*f*) Modulus of the difference of the two averages shown in (*a*) and (*b*) after alignment analog to (*e*). All frames are 25 nm wide. Full gray scale corresponds to 1.0 nm in (*a*), 1.0 nm in (*b*), 0.3 nm in (*c*) and (*d*), 1.0 nm in (*e*) and 0.5 nm in (*f*).

its fast scan direction appeared to be correlated with the tip quality. Thus, tips were selected for minimal stick-and-slip behavior. Randomly adsorbed small particles often helped to identify tip-induced oriented structures, and multiple tip effects were frequently revealed at edges.

Moreover, as documented in Fig. 8, the tip geometry changed during imaging. Therefore, techniques to assess the tip geometry in situ, i.e., when acquiring topographs, had to be developed. One approach was to simply analyze the structural features of topographs from one specimen area. For example, the porin crystal in Fig. 8 *a* showed the correct lattice lines but had a unit cell morphology lacking the threefold symmetry expected for porin trimers. During the next scan pronounced instabilities occurred, but the image became stable toward the end of the frame (Fig. 8 *b*). This situation did not change for more than 1 h of continuous scanning as illustrated in Fig. 8 *c*. The topographs reproducibly unveiled a trimeric unit arranged in a rectangular lattice, with no spurious structures related to the fast scan direction, nor any astigmatism. The image became fuzzy after 2 h of scanning, revealing unit cells that could not be interpreted (Fig. 8 *d*). High-quality images allowed the tip radii to be estimated from the depth and width of individual pores (Fig. 9 *a*). The porin channel was approximated by a cylinder and the tip by a sphere (Fig. 9 *b*). Radii of the tip that was used to record Figs. 5, 6, and 7 were evaluated from several pores and are displayed as a histogram in Fig. 9. The average tip radius was found to be 2.2 ± 0.2 nm ($N = 152$). Since no differences between trace and retrace topographs were detected, and the lateral displacement between trace and retrace frames was typically 6 pixels (for 512 × 512-pixel frames), corresponding to 2.4 nm in Figs. 5, 6, and 7 in the fast scan direction (no offset in the slow direction), we conclude that the identical tip at the apex of the pyramid was making the contact for both scan directions rather than different microtips.

As observed previously, the extracellular side of OmpF porin revealed a critical sensitivity to the applied force (Schabert et al., 1994). Using oxide-sharpened Olympus tips at forces of ~100 pN enabled stable imaging over periods of >1 h (Fig. 3 *d*). Increasing the applied force to 300 pN when scanning over terraces between single and double layers re-

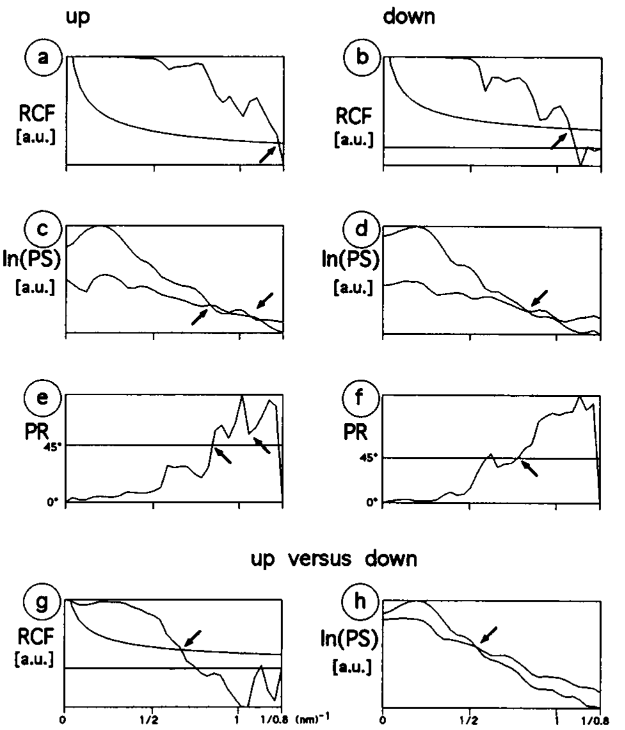

FIGURE 7 Assessment of the lateral resolution by different criteria. The porin averages of the up and down orientations shown in Fig. 6 were used to calculate RCF of two independent subaverages. (*a*) The RCF of the up orientation reveals a resolution of 0.8 nm (arrow). (*b*) same as in (*a*) for the down orientation, exhibiting a resolution of 0.9 nm (arrow). (*c*) The spectral signal power of the up orientation compared with the fourfold spectral noise power. Significant information is present beyond a resolution of 1 nm (right arrow). (*d*) Same as in (*c*) for the down orientation. The resolution extends to 1.2 nm. (*e*) The PR calculated from the independent transforms of the up orientation crosses the 45° threshold at 1.2 nm^{-1}, but recovers to 50° twice, suggesting valuable information at 0.9 nm^{-1} (right arrow). (*f*) same as in (*e*) for the down orientation. (*g*) The RCF of up and down averages crosses the noise threshold at 1.5 nm^{-1} consistent with the highest discernible diffraction order (5.0, corresponding to 1.6 nm^{-1}) after unbending (Fig. 5). (*h*) The spectral noise calculated from up and down averages after angular alignment is significantly higher than that of individual independent averages. Therefore the spectral power crosses the noise limit at 1.8 nm^{-1}. The units of the x axis are nm^{-1}.

sulted in a displacement of the upper layer and a concomitant exposure of the lower layer. However, only bilayers that were lacking the two loosely bound LPS molecules per trimer could be separated. Forces and scan speeds equivalent to those reported for the dissection of gap junctions (10 nN, up to 20 μm/s) (Hoh et al., 1991) led to a disruption of both layers. The periplasmic side proved to be more stable than the extracellular side. Deformations were observed only for forces >500 pN and occurred more likely at edges and crystal defects.

The bandwidth of the AFM is limited by the stiffness of the sample, the viscosity of the buffer, the cantilever, and the bandwidth of piezo and feedback loop (Butt et al., 1993). Therefore, the feedback gains and the scan speed have to be properly adjusted for tracing the topography of the sample with the tip at high resolution. As demonstrated in Fig. 10, reducing the bandwidth of the AFM feedback resulted in an increase of the deflection signal (Fig. 10, *b*, *d*, and *f*), while the corresponding corrugation amplitude was reduced (Fig. 10, *a*, *c*, and *e*). Resetting the gains to their optimal values allowed the previous corrugation amplitude to be recovered, demonstrating that deformations of the structure were elastic. As higher feedback gains induced oscillations, the practical scan speed limit was ~1 μm/s, lower than that expected from a theoretical analysis of the cantilever properties (Butt et al., 1993).

Lattice transformations

OmpF porin trimers reconstituted in the absence of loosely bound LPS molecules usually assembled into rectangular lattices with $a = 8$ and $b = 14$ nm. Occasionally, periplasmic sides also revealed a hexagonal lattice with $a = b = 22$ nm that was surrounded by the rectangular lattice (marked in Fig. 11 *b*). The averages of both lattices are shown in the insets of Fig. 11 *b*. In the transition zone between the rectangular and hexagonal crystal intermediate packing arrangements of the trimers can be discerned (Fig. 11 *a*). Depending on the reconstitution conditions, five different 2D crystallographic packing arrangements have been reported for OmpF porin (Dorset et al., 1983, 1989; Hoenger et al., 1990; Jap et al., 1992), but the arrangement shown here has not been reported before. It can be generated from the rectangular lattice by eliminating every third trimer along lattice lines parallel to lattice vector **b** and some reorientations of the remaining trimers.

DISCUSSION

The goal of this study was to establish conditions that allow OmpF porin crystals to be imaged reproducibly at subnanometer lateral resolution. To this end, the requirements for high-resolution imaging of biological membranes by AFM were systematically analyzed.

As a result of electrostatic interactions OmpF porin crystals were stably immobilized on freshly cleaved mica substrates in the presence of Mg^{2+} ions in a perfectly planar configuration. In contrast to this, porin sheets that were covalently linked to modified glass substrates were stable for imaging, but not sufficiently flat to achieve high resolution. It is conceivable that the porin membranes did not spread on the slightly hydrophobic glass surface (Karrasch et al., 1993) and were covalently linked to it in a wrinkled conformation.

Tip size and geometry are the critical factors limiting the resolution of all scanning probe microscopes. Therefore, electron microscopy has been used to characterize the tips. Silicon tips (Ultralever, Park Scientific Instruments, CA) were reported to have tip radii of 3.7 nm in the best case (Tortonese et al., 1994) and typically 10 nm (Ultralever, Park Scientific Instruments, CA; Nanoprobe, Olaf Wolter, Wetzlar, Germany). Nevertheless, high-resolution topographs of HPI layer were obtained reproducibly with standard $\mathrm{Si_3N_4}$ tips (Karrasch et al., 1993, 1994) suggesting tip radii of <5 nm. The discrepancy between the radii determined by electron microscopy and by in situ analysis is difficult to explain because contrast and resolving power

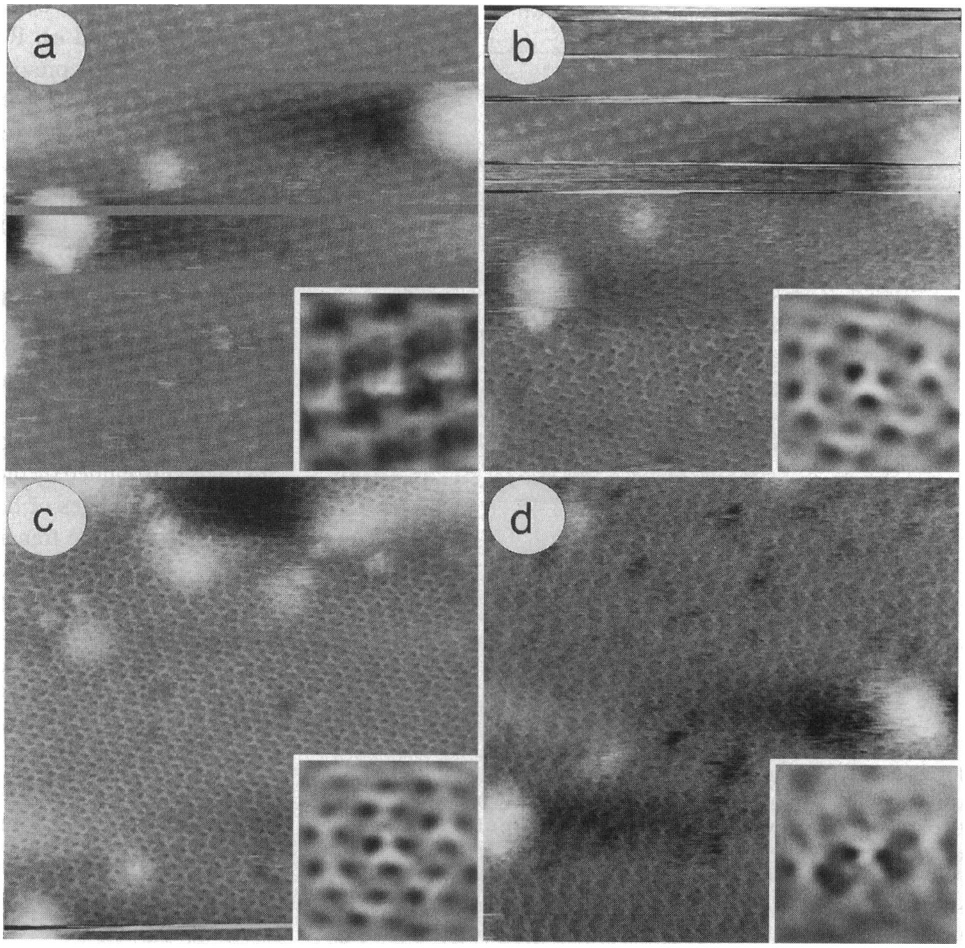

FIGURE 8 Tip changes during scanning. A sequence of AFM topographs reveals different morphologies due to alterations of the tip. Shown are images of the periplasmic side of the reconstituted rectangular porin crystal without loosely bound LPS molecules. The topographs have been corrected for friction, and averages were calculated by single-particle averaging. (*a*) Topograph and average (inset) of a first scan at high magnification. A few distorted scan lines were removed. (*b*) The next scan reveals a drastic change in the morphology and in the average (inset), calculated from the lower part. (*c*) The morphology of the periplasmic side after acquisition of five further topographs acquired at approximately the same position and the corresponding average (inset). (*d*) After 2 h of scanning, the topograph changed again. A different morphology is visible in the average (inset), which was stable over a series of images. All frames are 200 nm wide and all insets are 25 nm wide.

of the former are sufficient to visualize subnanometer structures. However, this discrepancy emphasizes the need to efficiently select individual tips in situ. Furthermore, drastic changes of the topographs within a few scans demonstrated alterations of the tips during imaging and document the necessity of an in situ assessment of the tip quality. Colloidal gold particles that have been employed as standard to evaluate the tip structure at ambient pressure (Vesenka et al., 1993) would have to be immobilized for scanning in solution. Therefore, an estimate of the tip structure in situ by analyzing characteristic features within the specimen is preferred.

We have found that reducing the applied force to ~100 pN ensured reproducible imaging of the rather flexible extracellular side of porin trimers over hours. The periplasmic side was much more stable, withstanding forces up to 500 pN, probably as a result of the complete integration in the periplasmic leaflet of the bilayer. Together with image instabilities at edges and lattice defects this suggests that shear forces rather than forces normal to the membrane are responsible for sample deformations. We have used 120 μm-long cantilevers because longer and therefore softer cantilevers exhibited a lack of lateral stability. This suggests that the resolution achieved on biological membranes may be

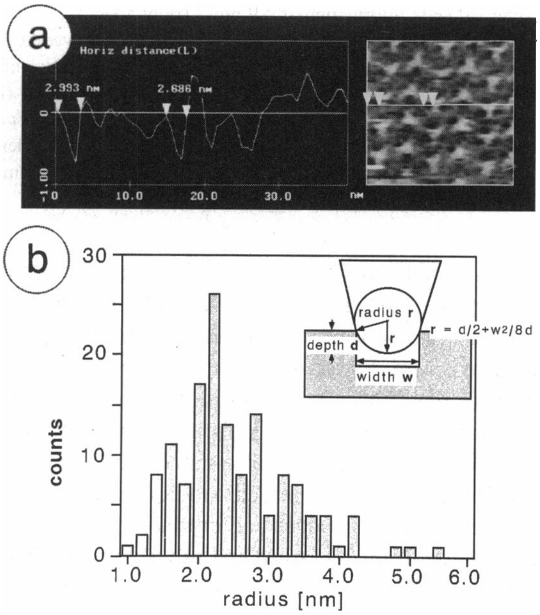

FIGURE 9 Tip radius assessed from scans over cylindrical channels. (*a*) Topographs of the periplasmic side of porin with only one tightly bound LPS molecule/trimer. Width and depth of the pores are compared within the same scan line. (*b*) Histogram of the tip radii measured for an oxide-sharpened tip. The model used for the calculation of the radii is shown in the inset.

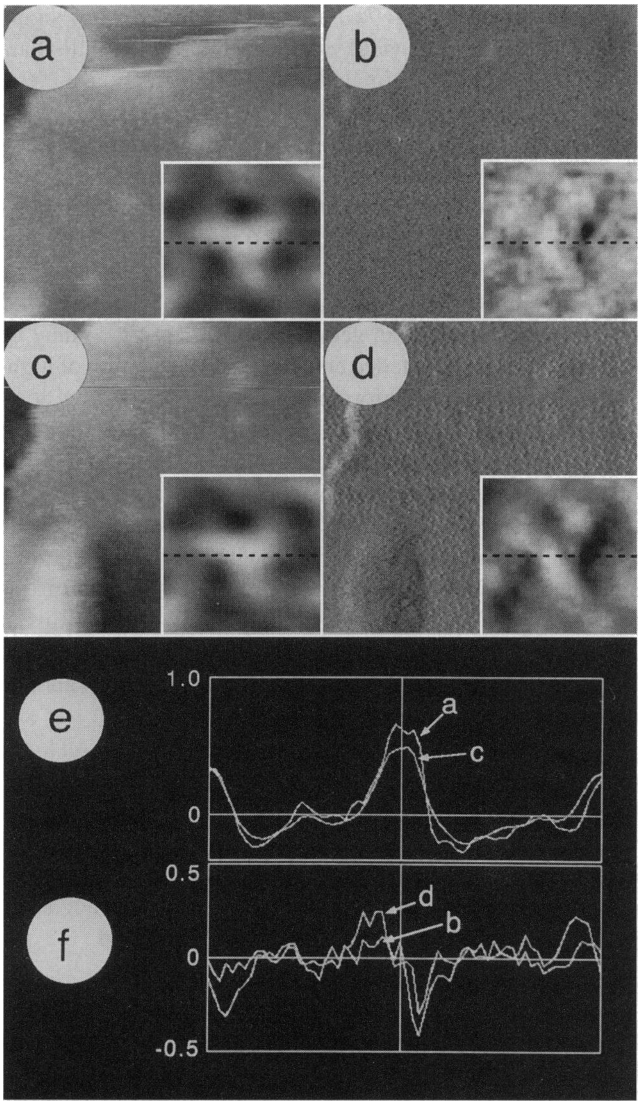

FIGURE 10 Bandwidth versus contrast. (*a*) Shows the topograph of the periplasmic side of a porin crystal that was reconstituted with two loosely bound LPS molecules/porin trimer and the single particle average (inset). (*b*) The deflection signal, which was acquired simultaneously with (*a*). The inset shows the single-particle average that was calculated corresponding to the inset in (*a*). (*c*) The same position as in (*a*) was recorded with the gains of the feedback reduced to half of the value as in (*a*). (*d*) Deflection signal simultaneously acquired with (*c*). The average was calculated analogously to (*c*). (*e*) Height profile through the center of the averages in (*a*) and (*c*). (*f*) Horizontal traces as marked in the averages in (*b*) and (*d*). Scan size is 220 nm for (*a*–*d*). The width of the averages and the sections is 13 nm.

improved by cantilevers that are soft in the direction of the *z* axis but rigid with respect to the torsion induced by friction effects. It should be noted that the forces reported here are nominal values calculated from the spring constants provided by the manufacturers. A more detailed analysis of the applied forces requires the calibration of individual cantilevers (Butt et al., 1993; Cleveland et al., 1993).

Prerequisites for the quantitative analysis of friction are simultaneously acquired trace and retrace images and the absence of topography changes (Grafstöm et al., 1993, 1994; Radmacher et al., 1992; Schabert et al., 1994). Therefore,

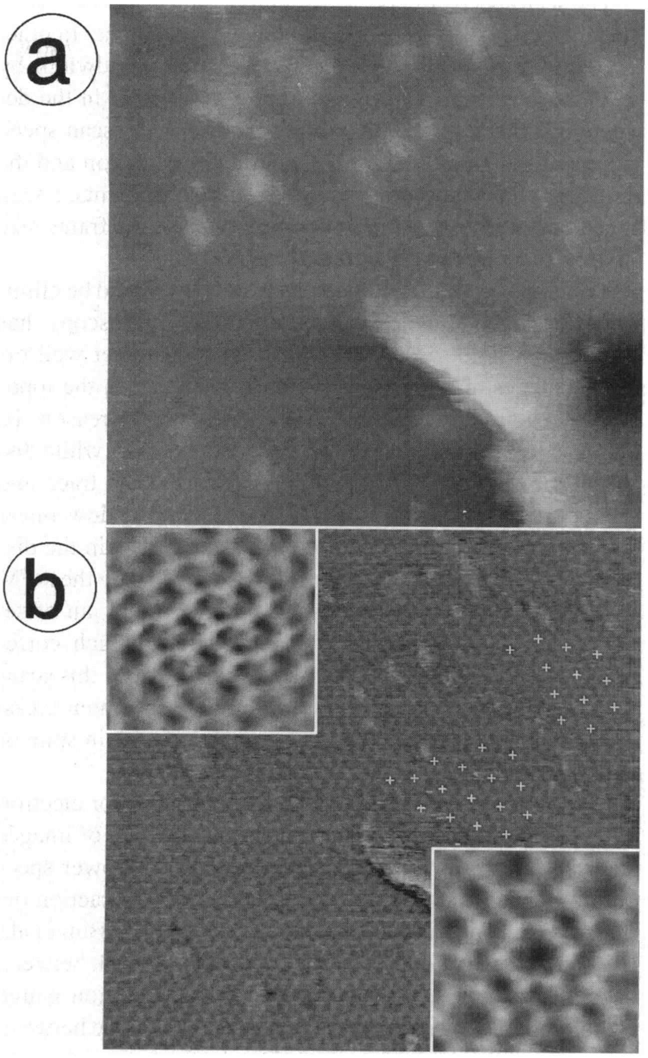

FIGURE 11 Phase transitions in OmpF porin lattices. OmpF porin reconstituted with a single tightly bound LPS molecule/trimer at an LPR of 0.2 assembled into a rectangular lattice with $a = 8$ nm, $b = 14$ nm, but also revealed areas with a hexagonal lattice $a = b = 22$ nm, and transitions between the two lattices. (*a*) Unprocessed topograph of the periplasmic side. (*b*) The topograph shown in (*a*) was high-pass filtered and the position of hexagonal unit cells are marked. The corresponding average is shown in the inset (bottom right), whereas the average of the rectangular lattice is shown in the top left inset. (The frame size is 395 nm for (*a*) and (*b*). Both insets have a width of 50 nm. The full gray scale corresponds to 10 nm in (*a*).

friction cannot be assessed quantitatively on soft samples such as biological membranes by the difference method. Whereas 2D lipid protein crystals provided sufficient stability to withstand the frictional forces present in contact-mode AFM, the fluid-phase lipid membranes could not be imaged at high resolution. For investigation of noncrystalline biological membranes, either the absence of friction or a high-protein density where protein-protein contacts increase the lateral stability is therefore required. Friction effects occurring in the contact AFM, however, may be eliminated by the use of noncontact or tapping techniques (Elings and Gurley, 1993; Hansma et al., 1993), which appear to work also in solution (Hansma et al., 1994; Putman et al., 1994).

The scan speed affects the resolution (Butt et al., 1993) and also influences the measured corrugation amplitude. In practice, the scan speed can be adjusted to the bandwidth by reducing the speed until no structures are visible in the deflection signal anymore. The lower limit for the scan speed is given by thermal drift of the cantilever deflection and the time for acquiring a single frame. In our experiments, a scan speed of ~4 lines/s yielding a speed <1 μm/s for frame size smaller than 250 nm was found to be adequate.

All images exhibited lattice distortions that could be eliminated by unbending. However, electron microscopy has shown that 2D porin crystals are in general rather well ordered, suggesting that the distortions observed in the topographs acquired by AFM may have some specific reason. To identify the latter, porin membranes were scanned while disabling the slow scan direction, acquiring data in trace and retrace mode (data not shown). This allowed a slow linear drift (3 nm/min) to be measured that would explain the discrepancy between the lattice vectors determined by the AFM and data from electron microscopy. Furthermore, an offset ripple of ~1-nm amplitude became visible, which corresponds to the resolution of the j-scanner. But since this scanner allowed an efficient search for suitable specimen areas, it was used for collecting the data presented here in spite of this noticeable limitation.

Digital image processing methods developed for electron microscopy are becoming popular for the analysis of images recorded by scanning probe microscopes. The power spectrum of periodic structures revealing distinct diffraction orders gives one possibility to assess the resolution (Butt et al., 1990), while the width of the cross-correlation peak between trace and retrace scans has been used as resolution gauge (Tillmann et al., 1992). In the latter case a tip change between the two scan directions is assumed to eliminate the influence of the tip geometry. Furthermore, the commonly used Fourier RCF (Saxton and Baumeister, 1982) or the Fourier ring PR (Frank et al., 1981) have been calculated to evaluate different images recorded by STM and AFM (Butt et al., 1992). In this latter work it was concluded that both the RCF and the PR overestimate the resolution of SPM images as a result of their high signal-to-noise ratio, and the resolution limit has been defined as the frequency where the signal power falls below 10% of the average power calculated within the frequency range above which the signal drops systematically.

The wealth of data presented here allows us to reconsider the question of resolution in SPM. First, the reproducibility of the height measurements, i.e., the vertical resolution, can be evaluated with a precision that is limited by the precision of the lateral and angular alignment of identical unit cells or macromolecules, i.e., the lateral resolution. As noted previously (Karrasch et al., 1994), the RMS map $\sigma_{k,l}$ reveals areas of the structure that exhibit high fluctuations, a piece of information that may be of biological significance. In contrast, areas that are more rigid exhibit smaller values $\sigma_{k,l}$ and allow an estimate of the ultimate vertical resolution. In addition, the rigid parts of the structure may subsequently be used to refine the alignment of the individual unit cells.

As illustrated in Fig. 7, *a–f*, the RCF, the spectral signal power, and the PR all yield values for the resolution that are better than what is estimated from the diffraction pattern, even after unbending the crystal. The comparison of the topographs of porin trimers in up and down orientations, however, reveals a resolution of 1.5 nm (RCF) and 1.8 nm (spectral signal power), respectively. The latter result is compatible with the resolution of 1.6 nm estimated from the highest visible diffraction order. According to this analysis, a deconvolution of porin trimer images to a resolution of 1 nm using appropriate tip geometries (Keller, 1991) may be feasible. This is expected to enhance the contribution of high-frequency structural information lost in the strong low-frequency components typically present in AFM topographs.

As expected from the high resolution and reproducibility of the topographs, features of the periplasmic and the extracellular sides can be interpreted and correlated with the x-ray data. Identification of LPS molecules would require a systematic investigation of porin lattices comprised of different OmpF-LPS isoforms with well-characterized tips at identical resolution. However, our present data suggest that the flexible saccharides are pushed away by the stylus and do not therefore produce a discernible signal.

A novel crystal-packing arrangement and its transition to the more abundant rectangular crystal form was observed. This large hexagonal form ($a = b = 22$ nm) is atypical for a reconstitution with an LPR of 0.2, as a low LPR usually results in a tighter crystal packing. Nevertheless, this observation illustrates that crystal defects and transitions between different crystallographic packing arrangements are distinguished by the AFM.

CONCLUSIONS

Here we report on the conditions to record subnanometer-resolution topographs of OmpF porin crystals in solution. Limiting factors are discussed and techniques to characterize the tips are presented. The data that were acquired with commercial tips and instruments are an important step toward the structural analysis of native (non-crystalline) biological membranes, since techniques that overcome resolution limits imposed by the lack of crystal order by taking advantage of the high signal-to-noise ratio have been demonstrated.

The authors are grateful to Dr. Andreas Hoenger for the reconstituted OmpF porin lattices, to Dr. Reiner Hegerl (MPI for Biochemistry, Martinsried, Germany) for the unbending program, to Christian Henn for the model of the OmpF porin trimer, and to Dr. Cora-Ann Schoenenberger for discussing this manuscript. This work was supported by the Swiss National Foundation for Scientific Research, grant 31-32536.91 to A. E.; and by the Department of Education of Basel-Stadt, the Research Foundations of Ciba-Geigy, Hoffmann-La Roche and Sandoz, and the Maurice E.-Müller Foundation of Switzerland.

REFERENCES

Amrein, M. 1989. STM on freeze-dried and Pt-Ir-C coated bacteriophage T4 polyheads. *J. Ultrastruct. Mol. Struct. Res.* 102:170–177.

Binnig, G., and C. F. Quate. 1986. Atomic force microscope. *Phys. Rev. Lett.* 56:930–933.

Binnig, G., and H. Rohrer. 1982. Scanning tunneling microscope. *Helv. Phys. Acta.* 55:726–735.

Butt, H.-J., K. H. Downing, and P. K. Hansma. 1990. Imaging the membrane protein bacteriorhodopsin with the atomic force microscope. *Biophys. J.* 58:1473–1480.

Butt, H. J., Guckenberger, R. and Rabe, J. P. 1992. Quantitative scanning tunneling microscopy and scanning force microscopy of organic materials. *Ultramicroscopy*. 46:375–393.

Butt, H. J., P. Siedle, K. Seifert, K. Fendler, T. Seeger, E. Bamberg, A. L. Weisenhorn, K. Goldie, and A. Engel. 1993. Scan speed limit in atomic force microscopy. *J. Microsc.* 169:75–84.

Cleveland, J. P., S. Manne, D. Bocek, and P. K. Hansma. 1993. A nondestructive method for determining the spring constant of cantilevers for scanning force microscopy. *Rev. Sci. Instrum.* 64:403–405.

Cowan, S. W., T. Schirmer, G. Rummel, M. Steiert, R. Ghosh, R. A. Pauptit, J. N. Jansonius, and J. P. Rosenbusch. 1992. Crystal structures explain functional properties of 2 *E. coli* porins. *Nature*. 358:727–733.

Dorset, D. L., A. Engel, M. Häner, A. Massalski, and J. P. Rosenbusch. 1983. Two-dimensional crystal packing of matrix porin, a channel forming protein in *Escherichia coli* outer membranes. *J. Mol. Biol.* 165:701–710.

Dorset, D. L., A. K. Massalski, and J. P. Rosenbusch. 1989. In-plane phase transition of an integral membrane protein: Nucleation of the OmpF matrix porin rectangular polymorph. *Proc. Natl. Acad. Sci. USA*. 86:6143–6147.

Drake, B., C. B. Prater, A. L. Weisenhorn, S. A. C. Gould, T. R. Albrecht, C. F. Quate, S. Cannell, H. G. Hansma, and P. K. Hansma. 1989. Imaging crystals, polymers, and processes in water with the atomic force microscope. *Science*. 243:1586–1589.

Engel, A. 1991. Biological application of scanning probe microscopes. *Annu. Rev. Biophys. Biophys. Chem.* 20:79–108.

Engel, A., A. Massalski, H. Schindler, D. L. Dorset, and J. P. Rosenbusch. 1985. Porin channel triplets merge into single outlets in *Escherichia coli* outer membranes. *Nature*. 317:643–645.

Frank, J., W., Goldfarb, D. Eisenberg, and T. S. Baker. 1978. Reconstruction of glutamine synthetase using computer averaging. *Ultramicroscopy*. 3:283–290.

Frank, J., A. Verschoor, and M. Boublik. 1981. Computer averaging of electron micrographs of 40 S ribosomal subunits. *Science*. 214:1353–1355.

Grafström, S., J. Ackermann, T. Hagen, R. Neumann, and O. Probst. 1994. Analysis of lateral force effects on the topography in scanning force microscopy. *J. Vac. Sci. Technol. B*. 12:1559–1564

Grafstöm, S., M. Neitzert, T. Hagen, J. Ackermann, R. Neuman, O. Probst, and M. Wörtge. 1993. The role of topography and friction for the image contrast in lateral force microscopy. *Nanotechnology*. 4:143–151.

Guckenberger, R., T. Hartmann, W. Wiegräbe, and W. Baumeister. 1991. The scanning tunneling microscope in biology. *In* Scanning Tunneling Microscopy, Vol. 2: Further Applications, and Related Scanning Techniques. R. Wiesendanger, H.-J. Güntherodt, editors. Springer-Verlag, Berlin.

Hansma, P. K., J. P. Cleveland, M. Radmacher, D. A. Walters, P. Hillner, M. Bezanilla, M. Fritz, D. Vie, and H. G. Hansma. 1994. Tapping mode atomic force microscopy in liquids. *Appl. Phys. Lett.* 64:1738–1740.

Hansma, H. G., R. L., Sinsheimer, J. Groppe, T. C. Bruice, V. Ellings, G. Gurley, M. Bezanilla, I. A. Mastrangelo, P. Hough, V. C. and Hansma, P. K. (1993). Scanning. 15:296–299.

Hoenger, A., R. Gosh, C. Schoenenberger, U. Aebi, and A. Engel. 1993a. Direct in situ structural analysis of recombinant outer membrane porins expressed in an OmpA-deficient mutant of *Escherichia coli* strain. *J. Struct. Biol.* 111:212.

Hoenger, A., J.-M. Pagès, D. Fourel, and A. Engel. 1993b. The orientation of porin OmpF in the outer membrane of *Escherichia coli*. *J. Mol. Biol.* 233:400–413.

Hoenger, A., H. Gross, U. Aebi, and A. Engel. 1990. Localization of the lipopolysaccharides in metal-shadowed reconstituted lipid-porin membranes. *J. Struct. Biol.* 103:185–195.

Hoh, J. H., R. Lal, S. A. John, J.-P Revel, and M. F. Arnsdorf. 1991. Atomic force microscopy and dissection of gap junctions. *Science*. 253:1405–1408.

Hoh, J. H., G. E. Sosinski, J.-P. Revel, and P. K. Hansma. 1993. Structure of the extracellular surface of the gap junction by atomic force microscopy. *Biophys. J.* 65:149–163.

Jap, B. K., M. Zulauf, T. Scheybani, A. Hefti, W. Baumeister, U. Aebi, and A. Engel. 1992. 2D crystallization: from art to science. *Ultramicroscopy*. 46:45–84.

Karrasch, S., M. Dolder, F. Schabert, J. Ramsden, and A. Engel. 1993. Covalent binding of biological samples to solid supports for scanning probe microscopy in buffer solution. *Biophys. J.* 65:2437–2446.

Karrasch, S., R. Hegerl, J. H. Hoh, W. Baumeister, and A. Engel. 1994. Atomic force microscopy produces faithful high-resolution images of protein surfaces in an aqueous environment. *Proc. Natl. Acad. Sci. USA*. 91:836–838.

Keller, D. 1991. Reconstruction of STM and AFM images distorted by finite-size tips. *Surface Science*. 253: 353–364.

Manne, S., P. K. Hansma, J. Massie, V. B. Elings, and A. A. Gewirth. 1991. Atomic-resolution electrochemistry with the atomic force microscope: copper deposition on gold. *Science*. 251:183–186.

Putman, C. A. J., K. Van der Werft, B. G. De Grooth, N. F. Van Hulst, and J. Greve. 1994. Tapping mode atomic force microscopy in liquid. *Appl. Phys. Lett.* 64:2454–2456.

Putman, C. A. J., K. O. van der Werft, B. G. de Grooth, N. F. van Hulst, J. Greve, and P. K. Hansma. 1992. A new imaging mode in the atomic force microscopy based on the error signal. *SPIE* 1639:198–204.

Radmacher, M., R. W. Tilmann, M. Fritz, and H. E. Gaub. 1992. From molecules to cells: imaging soft samples with the atomic force microscope. *Science*. 257:1900–1905.

Saxton, W. O., and W. Baumeister. 1982. The correlation averaging of a regularly arranged bacterial cell envelope protein. *J. Microsc.* 127:127–138.

Saxton, W. O., W. Baumeister, and M. Hahn. 1984. Three-dimensional reconstruction of imperfect two-dimensional crystals. *Ultramicroscopy*. 13:57–70.

Saxton, W. O., R. Dürr, and W. Baumeister. 1992. From lattice distortion to molecular distortion: characterising and exploiting crystal deformation. *Ultramicroscopy*. 46:287–306.

Saxton, W. O., T. J. Pitt, and M. Horner. 1979. Digital image processing: the SEMPER system. *Ultramicroscopy*. 4:343–354.

Schabert, F., J. H. Hoh, S. Karrasch, A. Hefti, and A. Engel. 1994. Scanning force microscopy of *E. coli* OmpF porin in buffer solution. *J. Vac. Sci. Technol. B*. 12:1504–1507.

Stemmer, A., A. Hefti, U. Aebi, and A. Engel. 1989. Scanning tunneling and transmission electron microscopy on identical areas of biological specimens. *Ultramicroscopy*. 30:263–280.

Tillmann, R. W., M. Radmacher, and H. Gaub. 1992. Surface structure of hydrated amorphous silicon oxide at 3-angstrom resolution by scanning force microscopy. *Appl. Phys. Lett.* 60:3111.

Tortonese, M., Y. Chen, and M. D. Kirk. 1994. Sharp, high aspect ratio tips for high resolution atomic force microscopy. *PSI Probe*. In press.

Unser, M., B. L. Trus, and A. C. Steven. 1987. A new resolution criterion based on spectral signal-to-noise ratios. *Ultramicroscopy*. 23:39–52.

Vesenka, J., S. Manne, R. Giberson, T. Marsh, and E. Henderson. 1993. Colloidal gold particles as an incompressible atomic force microscope imaging standard for assessing the compressibility of biomolecules. *Biophys. J.* 65:992–997.

Yang, J., J. Mou, and Z. Shao. 1994a. Molecular resolution atomic force microscopy of soluble proteins in solution. *Biochim. Biophys. Acta*. 1199: 105–114.

Yang, J., J. Mou, and Z. Shao. 1994b. Structure and stability of pertussis toxin studied by in situ atomic force microscope. *FEBS Lett.* 228:89–92.

Yang, J., L. K. Tamm, W. T. Tillack, and Z. Shao. 1993. New approach for atomic force microscopy of membrane proteins. *J. Mol. Biol.* 229:286–290.